High-energy channeling implants of phosphorus along the silicon [100] and [110] axes

V. Raineri, R. Setola,* F. Priolo, and E. Rimini
Dipartimento di Fisica, Corso Italia 57, I-95129 Catania, Italy

G. Galvagno
Istituto di Metodologie e Tecnologie per la Microelettronica, Consiglio Nazionale delle Ricerche, Corso Italia 57, I-95129 Catania, Italy

(Received 29 May 1991)

Phosphorus ions in the energy range 0.25–1 MeV and in the dose range 2×10^{12}–1×10^{15} P/cm^2 were implanted along the [100] and [110] directions on Si single crystals or along a random direction (7° tilt and 23° twist angles). Some implants were performed also on Si samples with a 2-μm-thick surface amorphous layer to obtain truly random conditions. Profiles were obtained either by secondary-ion mass spectrometry or by spreading-resistance analyses after a rapid-thermal-annealing procedure. The presence of channeling tails in the so-called random implants in Si single crystals, due to feeding-in effects, is demonstrated and studied. In the channeling implants, the maximum penetration and the electronic stopping were determined as a function of the beam energy and axial direction. Furthermore, by increasing the implanted dose the dechanneled fraction was correlated with the number of displaced silicon atoms. All the obtained profiles were compared with Monte Carlo simulations using the MARLOWE code. A simple description of the electronic energy loss within different channels by a modified Oen-Robinson formula provided an excellent agreement between the calculated and the experimental profiles.

I. INTRODUCTION

The range of energies used in monoenergetic ion bombardment of semiconductors has gradually increased in recent years. Currently, the semiconductor industry, the preeminent industrial user of ion implanters, has a variety of machines capable of implanting a wide range of ions in the energy range 10–400 keV. Sophisticated end stations to control the wafer orientation with respect to the ion-beam direction within 0.1° or less are just available in the market. With the drive for the very large scale integrated (VLSI) complementary metal-oxide semiconductor (CMOS), for instance, the n-well isolation between devices has become a necessity and deep implants are a means of achieving this goal.[1] These deep implants require ion energies of the order of 1 MeV.[2] Channeling implants at these energies offer the opportunity of obtaining flat profiles on a 3-μm depth scale by only one implant,[3] with a reduced thermal budget. The high versatile control of the ion beam's orientation to the device structure is used for the formation of lightly doped drains (LDD) in twin-well CMOS process. High-energy implants have several traditional applications, as after-gate implantation to reduce the number of masks, and quite a few additional applications which make use of deep MeV implanted structures. It is enough to mention the formation of buried layers, well structures, and retrograde profiles to improve the latch-up immunity and the field optimization.

The possibility of technological applications pushes research not only toward a characterization of the implanted profiles but also toward a better understanding of the physical phenomena involved in ion implantation. Therefore reliable models are necessary to simulate the process. Common analytical codes are not able to reproduce the profile of implanted materials in crystal silicon with the precision required, and most of the Monte Carlo simulations do not allow one to describe the target structure. The single-crystal structure of the substrate allows the channeling of the implanted ions with several consequences on the final depth profile. Several works were carried out on channeling implants in the early days; recently interest arose for several possible applications and basic aspects are considered.[4–6] Our aim in the present work is to study in detail the P channeling phenomena at high energies for different crystal orientations and to characterize the dechanneling fraction due to the damage produced by the implantation at high doses.

Much effort was spent in the past in extracting electronic stopping cross sections from different theoretical models and checking the validity of the different theoretical concepts.[7–9] However, although these models can fit the experimental data of implants very well in amorphous materials, they are not able to predict the channeling implanted profiles, because of the lack of knowledge of the electronic stopping cross sections that account for the channeling and feeding-in phenomena that occur in crystal targets. So far ion implantation has been effectively modeled on computers; it can be well described by a few parameters which reduce process development and implementation time by the use of simulations, at least for implants in amorphous structures or in single crystals along directions far from the main axes or planes. In this latter case feeding-in has been also described in terms of exponential channeling tails. Implants along axes or planes require instead a quite detailed description; an at-

 ©1991 The American Physical Society

tempt will be made in this paper to describe the profile of implanted ions in terms of a few parameters, too. Indeed knowledge of the mechanisms involved in the energy transfer of particles penetrating a crystal remains to be ascertained. Due to the lack of experimental data and to the complexity of the problem many questions concerning the channeling stopping remain open.

For channeled particles the contribution of elastic nuclear collisions is considerably reduced with respect to random ions and, in the energy range covered in this work, it can be completely neglected. In the electronic stopping (S_l) three different ion-velocity regimes, with different energy-loss processes, can be distinguished. In the high-velocity region ($v \gg Z^{2/3} v_B$, where Z is the atomic number and $v_B = 2.19 \times 10^8$ cm/s is the Bohr velocity), the incident ion is completely stripped and the ionization and electronic excitations of individual target atoms are the main source of energy loss. In this case the Bethe-Bloch theory successfully describes the process.[10] In the low-velocity region, $v < v_B$, both projectile and target atoms are practically neutral. The theories based on statistical models predict a stopping proportional to velocity.[11,12] In the intermediate-velocity region, competing mechanisms make a single-equation description of stopping impossible, and several approximations have to be made, leading to complex expressions requiring adjustable parameters. Two approaches are typically utilized. In the first, an impact-parameter-dependent formula was obtained.[13] In the second, a dielectric calculation of the energy loss, considering only the valence electrons, was performed.[14] However it is difficult to obtain experimental data immediately comparable with these models.[15] Our work is concentrated in the region 0.25–1 MeV and the data are either in the low-energy ($v < v_B$) region where $Se \propto \sqrt{E}$ or in the middle region. For these reasons we chose a single approach based on an impact-parameter-dependent formula. To describe the impact-parameter dependence of the electronic stopping we used a modified Oen-Robinson model in the MARLOWE code[16] (MARLOWE is a Monte Carlo program which accounts for the crystal structure of the target). Starting from these considerations we could set this program to be able to reproduce quite well the experimental profiles of P ions implanted along different axial directions of silicon single crystals.

II. EXPERIMENT

P ions were implanted in 1000 Ω cm *n*-type, Czochralski-grown, silicon single crystals of (100) and (110) substrate orientation with energies in the range 0.25–1 MeV and fluences in the range $2 \times 10^{12} - 1 \times 10^{15}$ P/cm^2. All the implants were performed using a 400-kV ion implanter. The phosphorus ions were implanted at 250 keV by singly charged ions, at 500 and 700 keV by doubly charged ions, and at 1 MeV by triply charged ions. Accuracy was maintained in avoiding contaminations. The beam divergence was less than 0.15° and was obtained by two slits, 5 mm in radius separated by a distance of more than 2 m. The uniformity of the implants was controlled by an electrostatic scan situated before the first slit. The samples were mounted onto a goniometer holder able to control the tilt angle with a step of 0.1° and the twist angle with a step of 0.02°. The average dose rate was maintained in the range $10^{11} - 10^{12}$ cm^{-2} s^{-1} to avoid sample heating. All channeling implants were performed aligning *in situ* the sample by means of 700-keV He^{2+} Rutherford backscattering and channeling.[17] Since the critical angle for He is smaller than for the heavier P ions, the crystal is still aligned when switching to the P beam. In some cases the implants were performed on 2-μm-thick amorphous layers obtained by ion self-implantation at energies in the range 0.5–1 MeV.

The crystalline perfection of the samples before and after the ion implantation process was determined by means of Rutherford backscattering spectrometry (RBS) in combination with the channeling effect by using a 2.0-MeV He^+ beam extracted by a van de Graaff generator. The disorder distribution was determined using an iterative procedure.[18]

P profiles were measured by secondary-ion mass spectrometry (SIMS) analyses carried out by using a 10-keV Cs^+ primary beam and a negative-secondary-ion detection in order to optimize the sensitivity to P. To allow measurements of P concentrations down to 5×10^{15}/cm^3, the samples were left under vacuum overnight to reduce the background level of H, and hence ^{30}SiH to as low as possible in order to eliminate interference between the ^{31}P and the ^{30}SiH signals. The rastered area was of 250×250 μm^2 and the diameter of the analyzed area was 60 μm. The raw data were quantified using an ion-implanted standard and the depth scales were obtained by measuring the sputtered crater depths by interference microscopy.

After implantation some samples were annealed using rapid thermal annealing (RTA) in a N_2 atmosphere at 1000 °C for 10 s. This treatment is able to activate all the implanted dopant and to avoid diffusion (15 nm is the calculated diffusion length[19]). SIMS analyses of as-implanted and annealed samples showed virtually identical P profiles, demonstrating also that the transient diffusion is negligible. Transient diffusion is a well-known phenomenon for B implants in Si (Ref. 20) and has also been observed in P implants in silicon, but in the latter case the effect is quite small.[21] For the deep implants of this work the effect is below the sensitivity of our measurements.

P profiles were measured also by spreading-resistance (SR) analyses performed on the annealed samples. The substrates were *n* type to reduce spilling effects,[22,23] with a resistivity of ≈1000 Ω cm, corresponding to a carrier concentration of $\approx 2 \times 10^{12}$ cm^{-3}. This allows the measurements of the implanted atomic concentration down to 5×10^{13} cm^{-3}. All samples were beveled at 34′. In these conditions and with a probe step of 5 μm the depth resolution was about 50 nm. All the angles were measured by an interferometric method resulting in an uncertainty of less than 2%. All data were taken at a probe load of 10 g. The SR data were analyzed by the multilayers algorithm using the computational procedure by Berkowitz and Lux.[24] Dopant density profiles were calculated from resistivity profiles using the standard ASTM F

723-82, based on the work of Thurber, Mattis, and Liu.[25]

No difference was observed between SIMS (of as-implanted samples) and SR profiles (of annealed samples). For this reason we will not distinguish between SIMS or SR profiles in the following discussion.

III. RESULTS AND DISCUSSION

A. Low-dose implants

In Figs. 1(a)–1(d) the SR profiles obtained for 0.25–1-MeV P implants at a dose of 2×10^{13} cm^{-2} in an amorphous layer, in (100) silicon at 7° tilt and 23° twist angles, and in channeling conditions along the [100] axis are shown. The 7° tilt and 23° twist angle direction has been chosen to simulate the random direction. The ranges obtained considering the peak positions for implants in the amorphous target and in random conditions in Si(100) single crystal are the same and correspond to 0.38, 0.62, 0.74, and 1 μm at energies of 0.25, 0.5, 0.7, and 1 MeV, respectively [as calculated from the profiles of Figs. 1(a), 1(b), 1(c), and 1(d)]. Nevertheless a sharp fall in the end of the range is observed in the profiles of the amorphous target while a small tail extends up to higher depths in the profiles of 7° tilt and 23° twist angles. The difference is obviously due to feeding-in phenomena that cannot be avoided for implants performed in crystal targets even when random directions are selected.[26] It is clear that to reproduce the form of the profiles implanted in crystals the description of the crystal structure must be included in the simulation code to account for the feeding-in component. In Table I the experimental longitudinal stragglings obtained by the spread at half height of the peak for implants in the amorphous target and in the crystal along a random direction are compared with those obtained by the MARLOWE code. Details on the MARLOWE calculations are reported in Sec. III C. At this stage it is sufficient to note that the agreement between experiment and theory is excellent.

In Figs. 1(a)–1(d) the implants in channeling conditions along the [100] axis at a dose of 2×10^{13} P/cm^2 are also reported. The profiles are quite flat with an abrupt drop at the maximum penetration region. Increasing the energy the channeled profiles become flatter. This is due

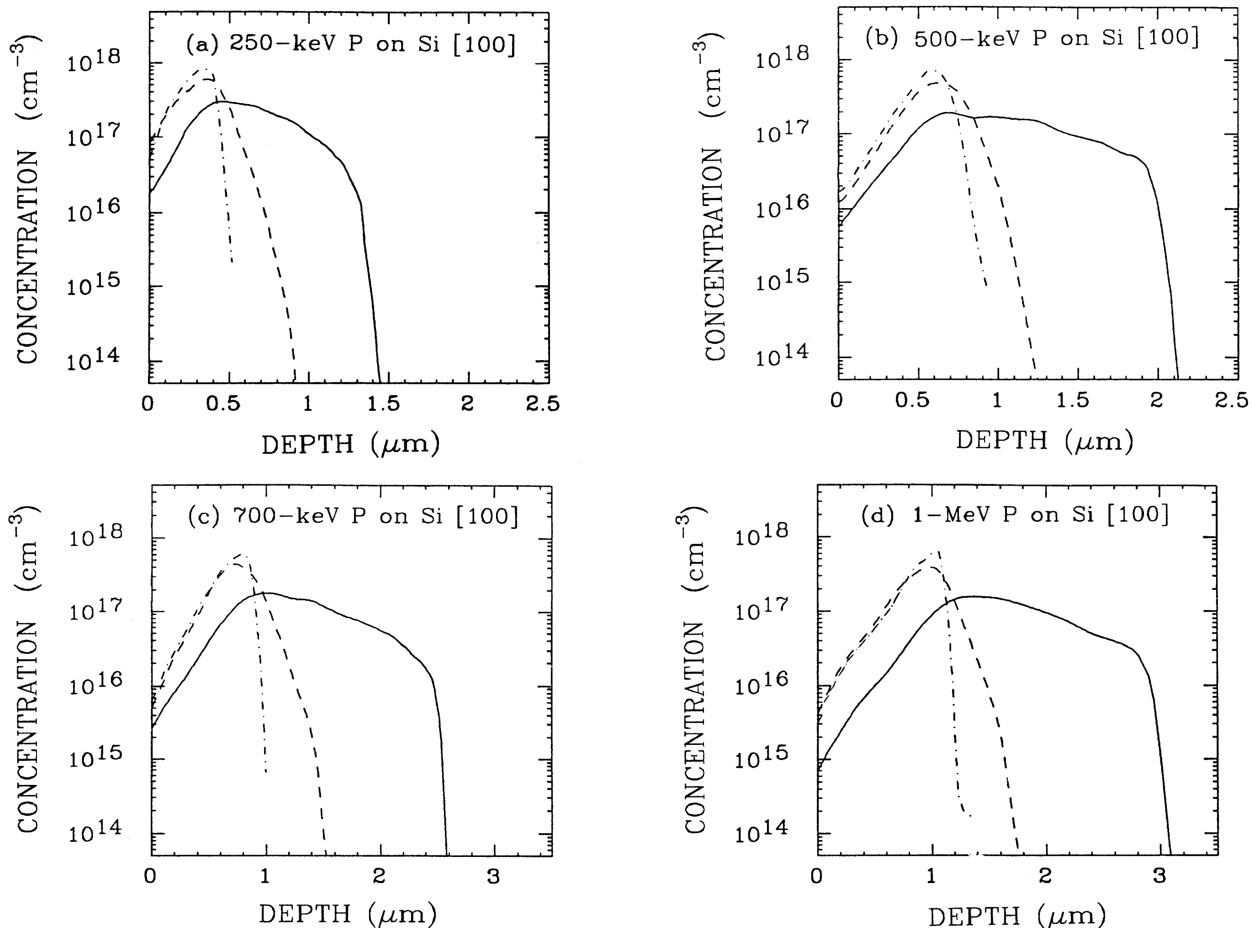

FIG. 1. Spreading resistance profiles of P implanted in Si at energies of (a) 250 keV, (b) 500 keV, (c) 700 keV, and (d) 1 MeV to a dose of 2×10^{13}/cm^2. The profiles refer to implants performed on (100) Si single crystal along a random direction (7° tilt angle and 23° twist angle) (dashed lines) and along the [100] axis (solid lines). Profiles of P implanted in a 2-μm amorphous layer (dash-dotted line) are also reported.

TABLE I. The longitudinal stragglings, experimental, and the distributions calculated by MARLOWE are reported. The values were obtained considering the spread at half height peak in the experimental and simulated profiles.

	Experimental		MARLOWE	
E (MeV)	ΔR_p(a-Si)	ΔR_p(c-Si)	ΔR_p(a-Si)	ΔR_p(c-Si)
0.25	0.29 μm	0.52 μm	0.29 μm	0.51 μm
0.50	0.48 μm	0.60 μm	0.46 μm	0.58 μm
0.70	0.53 μm	0.68 μm	0.53 μm	0.67 μm
1.00	0.59 μm	0.74 μm	0.58 μm	0.73 μm

to the saturation phenomena of the channeled fraction. For instance, at 1 MeV an almost flat profile at a concentration of $\approx 8\times 10^{16}/\text{cm}^3$ is distributed between 1 and 3 μm. The abrupt drop has the same shape as that of implants in amorphous targets. This is probably due to the fact that in both cases the energy is prevalently lost into electronic excitations. A random fraction is also present in these channeling implants and is determined by those ions entering the crystal close enough to the atomic row to be scattered by the outermost atoms to angles greater than the critical angle. We experimentally estimated this random fraction to be about 11% at all energies for implants along the [100] axis.

In Figs. 2(a)–2(c) profiles of P ions implanted in amorphous targets at different energies (0.25, 0.5, and 1 MeV) are again reported and compared with those obtained for implants in [110] silicon single crystals along the [110] axis. In the latter case SIMS profiles are shown. In these profiles two separate peaks are distinguishable. The first peak is at the same depth as the peak of the profile for ions implanted in random conditions and is due to the random fraction that we estimated to be $\approx 8\%$ of the implanted dose. The second peak corresponds to the channeled particles.

In channeling implants the maximum range ($R_{\max}$) is defined as the range of "well-channeled" particles moving along the centerline of the channel where the electronic density is at its minimum. At $R_{\max}$ therefore the particle distribution exhibits a rather sharp edge, beyond which the distribution drops off rapidly. We evaluated experimentally this maximum penetration depth $R_{\max}$ in all the channeled profiles at 1% of the channeled peak. The $R_{\max}$ obtained for all the energies are reported in Fig. 3 for both the [100] and [110] directions as a function of the square root of the energy. In both cases a linear trend is observed but the maximum penetration at the same energy is substantially deeper in channeling implants along the [110] axis. In the same figure the projected ranges obtained by implanting P in amorphous targets are also reported. In all cases the electronic energy loss is by far the principal energy-loss mechanism. However the large difference in penetration depth shows that the electronic density within the channel plays an important role and must be considered. This issue will be discussed in more detail in Sec. III C.

B. High-dose implants

The profiles obtained implanting P ions at 0.5 and 1 MeV and at increasing doses (up to $5\times 10^{14}/\text{cm}^2$) are shown in Figs. 4(a) and 4(b) for incidence along the [100] axis and in Figs. 5(a) and 5(b) for incidence along the [110] axis, respectively. As soon as the dose is increased the shape of the profiles changes. The channeled fraction, at high depths, is seen to saturate while a peak grows bigger and bigger at shallower depths. This result is the effect of damage which dynamically accumulates in the crystal as the implantation dose is increased, strongly increasing the dechanneling probability.

For simplicity the profiles can be considered as a sum of three contributions, one due to particles entering the crystal in a random direction, the second due to dechanneled ions, and the third due to the channeled particles. The random fraction of the beam is due to all those ions that impinge with the atomic row within the screening Thomas-Fermi radius, therefore suffering a large-angle scattering. Among the ions entering the channel only a few are well channeled and remain in the channel until they stop. These ions represent the channeled fraction. All ions that escape from the channel or are deviated and fed in planar channeling will contribute to the third component, the so-called dechanneled fraction. Increasing the implanted dose, the disorder introduced by ion implantation increases; then the dechanneled fraction component increases at the expense of the channeled fraction.

To determine experimentally the dechanneled fraction we used the procedure summarized in Fig. 6. From an implanted profile we subtracted the random profile associated with the fraction of incident ions which experiences a small impact-parameter collision with the atomic row of the crystal. For a random fraction we considered the profile implanted in the amorphous target scaled in such a way that the upper part of it coincides with the high-dose channeling profile. Again from the obtained profile we subtracted the channeled fraction that we supposed was given by the channeled profile obtained implanting the lower dose. This is of course an approximation but indeed we are subtracting a P channeling profile obtained on a perfect crystal, in the absence of appreciable damage. The profile which remained from the initial one after these two subtractions has been assumed to be the dechanneling profile. As an example of the adopted procedure the dechanneled components for 500-keV P implantation at different doses and along the [100] and [110] axes are drawn in Figs. 7(a) and 8(a).

In the same figures, 7(b) and 8(b), the profiles of the displaced silicon atoms, i.e., of the damage produced by the highest-dose P implant along the [100] and [110] channels are also reported. These profiles were extracted by an analysis of 2.0-MeV He^+ RBS spectra of the as-

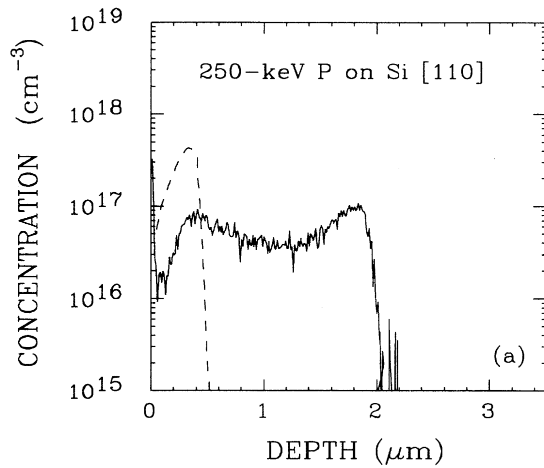

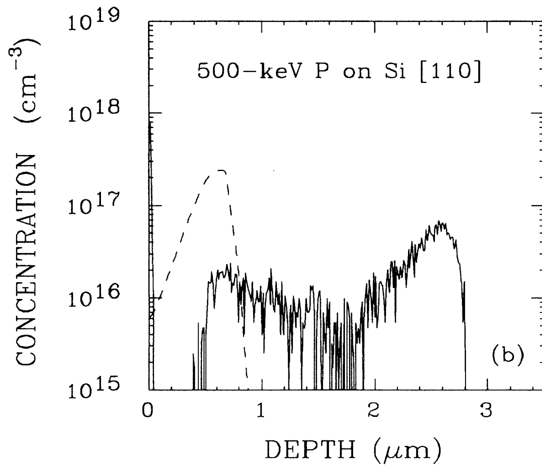

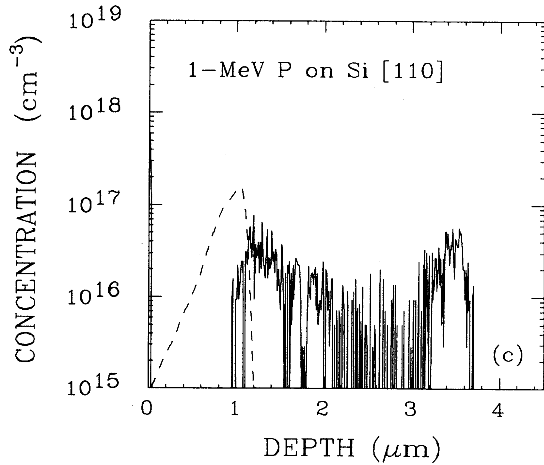

FIG. 2. SIMS profiles of P implanted on (110) oriented Si single crystal along the [110] direction (solid line) are compared with profiles implanted on a 2-μm-thick amorphous layer (dashed line). The profiles refer to implants performed (a) at 250 keV to a dose of $1\times10^{13}/cm^2$, (b) at 500 keV to a dose of $8\times10^{12}/cm^2$, and (c) at 1 MeV to a dose of $5\times10^{12}/cm^2$.

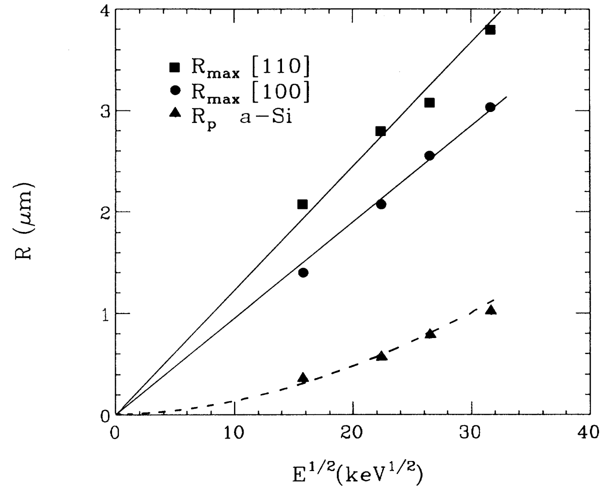

FIG. 3. Maximum penetration depth, R_{max}, as a function of the square root of the implantation energy for implants performed along the [100] and [110] Si axes. R_{max} has been extracted from the previous figures at 1% of the channeled peak. In the same figure the projected ranges extracted from the implants performed in thick amorphous layers are also reported.

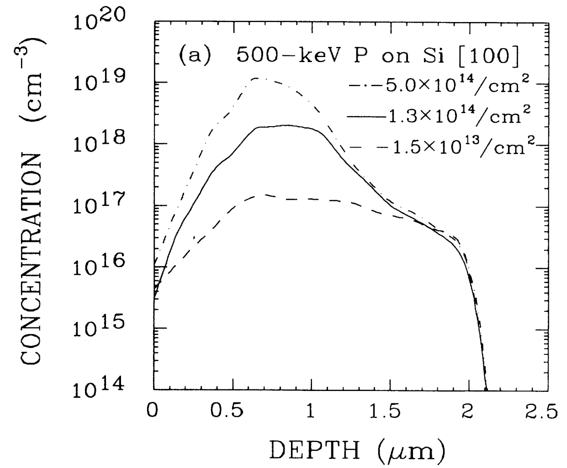

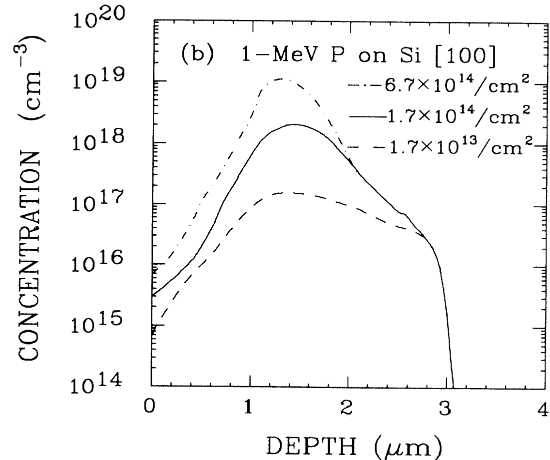

FIG. 4. P profiles for implants in channeling along the [100] axis (a) at 500 keV and (b) at 1 MeV and at increasing doses.

implanted samples. We supposed that the disorder can be described in terms of randomly displaced atoms. Assuming that the critical angle for channeling is unchanged by the introduction of disorder, that the flux of channeled particles is distributed uniformly within the channels, that all the displaced atoms can interact with the channeled particles, and that the dechanneled particles are not scattered back into channels, it is possible to determine the amount of dechanneling using an iterative procedure. The method compares the virgin spectrum, the damaged sample spectrum, and the random spectrum, and considers the dechanneling due to the disorder linearly added to the dechanneling that occurs in the crystal in the absence of disorder. This technique is commonly used in evaluating disorder in ion-implanted semiconductors. However when the disorder extends deep into the crystal it is difficult to follow the damage after the peak for concentrations lower than $\approx 10^{22}$ displaced atoms/cm^3.

The dechanneled fractions have an almost Gaussian profile with the peak position shifting toward the surface when increasing the implanted dose. These peaks are at the same depth of the peak of damage obtained by RBS measurements. From the RBS spectra the peak concentration of the displaced silicon atoms profiles was around 3×10^{21} cm^{-3} for the lower dose (1.3×10^{14} cm^{-2}) and

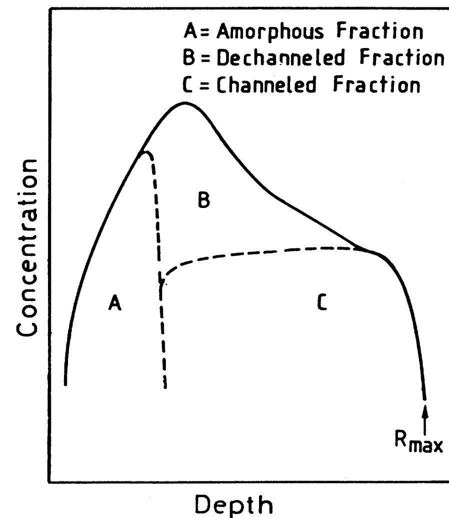

FIG. 6. Schematic representation of the procedure utilized to obtain the dechanneled fraction. A is the experimental random fraction obtained from the profile of implants in the amorphous target. C is the experimental channeled fraction obtained by a profile of low-dose implants in channeling conditions. The total profile less A and C is indicated as B and represents the experimental dechanneled fraction. The maximum penetration is also represented.

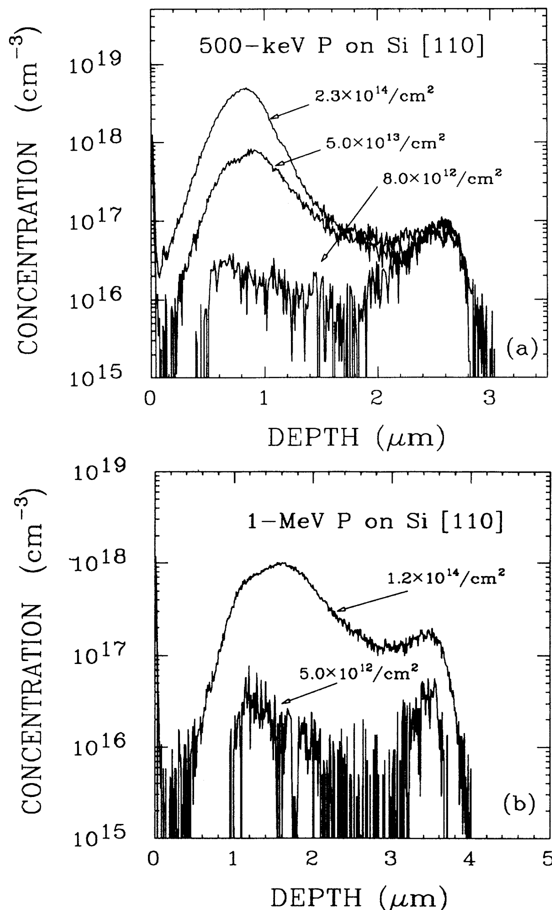

FIG. 5. P profiles for implants in channeling along the [110] axis (a) at 500 keV and (b) at 1 MeV and at increasing doses.

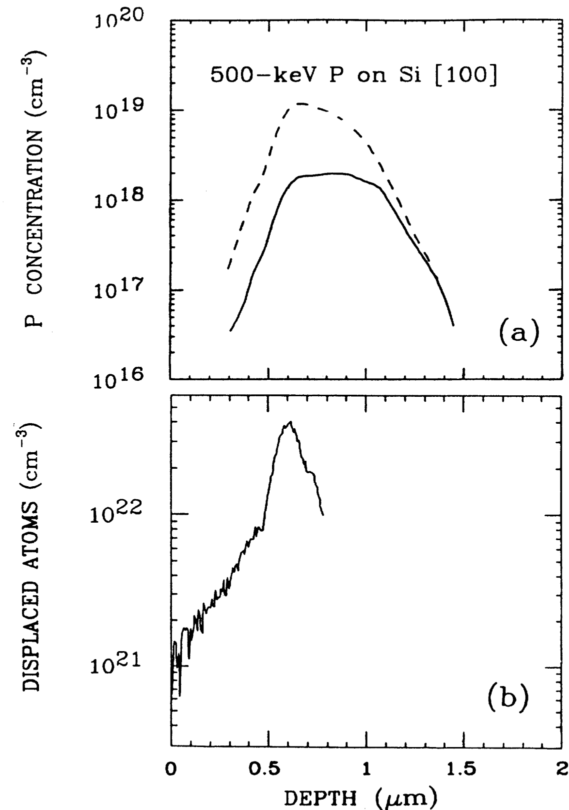

FIG. 7. The dechanneled profiles obtained as described in Fig. 6 are reported for 500-keV P implants along the [100] direction at the doses of 1.3×10^{14} and 5×10^{14}/cm^2 (a). For comparison the displaced atoms profile obtained by RBS and channeling for the 500-keV 5×10^{14} P/cm^2 as-implanted samples is reported in (b).

3.8×10^{22} cm^{-3} for the higher dose (5×10^{14} cm^{-2}) for implants along the [100] axis at 0.5 MeV [see Fig. 7(b)]. This means that the displacements per atom (DPA) range from 0.05 to 0.4 in this depth region. If we multiply the number of displacements/cm^2 for the [100] channel area we obtain the number of displacements in each channel. This number is 36 and 353 for the lower and higher dose, respectively. Furthermore all these displacements are concentrated in a depth range extending from 0.4 to 0.8 μm. It is evident that those particles which are initially channeled will be dechanneled in this region, where they will find one atom for every other 20 and one for every other 2 displaced from the regular lattice site for the low and high doses, respectively. This is consistent with the fact that the total number of channeled particles does not increase any more.

For the [110] direction [see Fig. 8(a)] again Gaussian profiles are obtained from the procedure previously described. In this case a wider damage distribution was obtained and as a consequence the profiles of Fig. 8(a) also extend up to 1.6 μm. The damage profile [Fig. 8(b)] extends up to 1 μm at a concentration still revealable by RBS measurements. The peak damage concentration is of 3.5×10^{22} displacements/cm^3 for an implanted P dose of 2.3×10^{14}/cm^2. The damage due to ion implantation in [110] channeling conditions is distributed in a larger region than for channeling implants along the [100] direction. However the displacements in every channel are more than enough to justify the saturation of the channeling component.

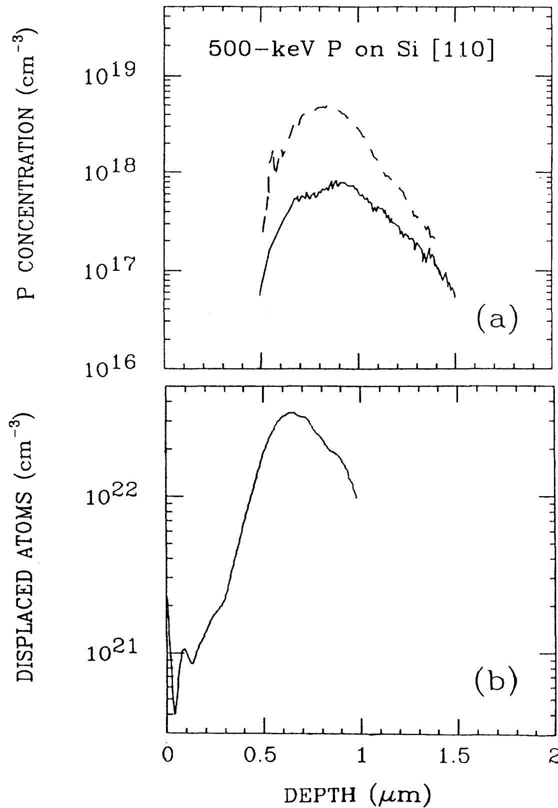

FIG. 8. The dechanneled profiles obtained as described in Fig. 6 are reported for 500-keV P implants along the [110] direction at the doses of 2.3×10^{14} and 5×10^{14}/cm^2 (a). For comparison the displaced atoms profile obtained by RBS and channeling for the 500-keV 5×10^{14} P/cm^2 as-implanted samples is reported in (b).

The numerical values of the random, channeled, and dechanneled fractions are summarized in Table II also for the other energies. From Table II it is clear that the channeled fraction increases with the ion implantation energy while the dechanneled fraction decreases. The random fraction for implants along the [110] channel is lower than for implants in the [100] direction, in agreement with the different dimensions of the channels.

C. MARLOWE simulations

Simulations of implanted profiles were obtained using the MARLOWE code.[27] This program uses a Monte Carlo approach to describe the trajectories of energetic ions both on crystalline and amorphous targets. In MARLOWE each particle trajectory is constructed as a series of two-body scattering from target atoms, and simultaneous collisions are treated in an approximate manner.[28] MARLOWE provides three choices for the interatomic potentials used in the nuclear scattering calculation. In our work we used the elastic nuclear scattering described by the Moliere potential:

$$V(r)=\frac{Z_1Z_2}{r}e^2\left[0.35\exp\left[\frac{-0.3r}{a}\right]+0.55\exp\left[\frac{-1.2r}{a}\right]+0.1\exp\left[\frac{-6r}{a}\right]\right], \quad (1)$$

where Z_1, Z_2 are the atomic numbers of the colliding particles (ion and target), e is the electron charge, and a is given by

$$a=\left[\frac{9\pi^2}{128}\right]^{1/3}a_B(Z_1^{1/2}+Z_2^{1/2})^{-2/3}, \quad (2)$$

a_B being the Bohr radius.

For the electronic stopping MARLOWE considers a

TABLE II. The random fraction, the channeled fraction, and the dechanneled fraction are reported for different doses at different energies and for channeling implants in different orientation.

E (MeV)	D (cm^{-2})	F_{ran}	F_{ch}	F_{dech}
		[100]		
0.5	1.3×10^{14}	10.4%	8%	81.4%
0.5	5×10^{14}	10.6%	2%	87.4%
1.0	1.7×10^{14}	10.6%	9.6%	79.8%
1.0	6.7×10^{14}	10.6%	2.4%	87%
		[110]		
0.5	5×10^{13}	7.5%	15%	77.5%
0.5	2.3×10^{14}	7.5%	3.5%	89%
1.0	1.2×10^{14}	7.5%	20%	72.5%

treatment for the local loss based on the Oen-Robinson approach, where the product of the Lindhard-Scharff-Schiott[29] stopping power and an exponential function of the impact parameter are used. However no dependence as a function of the channel is considered. We decided to use this approach for implants along the [100] channel, where the interaction of the incident ion occurs separately with only one atom at a time (see Fig. 9). The energy loss due to inelastic interaction with electrons is described by the impact-parameter-dependent formula:

$$Q_{[100]}(p,E)=Q(p,E)=\frac{s^2KE^{1/2}}{2\pi a^2}\exp\left[\frac{-sp}{a}\right], \quad (3)$$

being $K=\alpha K_L$, α a fitting parameter, p the impact parameter, and

$$K_L=\frac{1.216Z_1^{7/6}Z_2}{(Z_1^{2/3}+Z_2^{2/3})^{2/3}M_1^{1/2}}\ \mathrm{eV}^{1/2}\,\mathrm{\AA}^2 \quad (4)$$

the Lindhard-Scharff stopping power with M_1 the mass in amu of the incident ion. The value of α found in this work was 1.5.

The parameter s has been determined by Oen and Robinson to be 0.3.[30] Moreover by recent molecular orbital calculations,[31] and by local-electron-density calculations,[32] s ranges between 0.22 and 0.46 and increases with increasing energy. For P ions in the energy range of the present investigation the s value should be around 0.3. Considering s as an adjustable parameter we were able to fit the implanted profiles at all the energies with $s=0.315$

When the implanted ion moves along the [110] channel it will interact simultaneously with three atoms (see Fig. 10). In this case we used a corrected Oen-Robinson formula including the interaction with the three atoms simultaneously, i.e.,

$$Q_{[110]}(p,E)=Q(p,E)+Q(p',E)+Q(p'',E)\ . \quad (5)$$

In this case p is the impact parameter of the incident ion with atom 2, and p' and p'' are the distances with the other two atoms, 1 and 3 (see Fig. 10). A calculation of these distances for any possible configuration is difficult and not necessary. In a first approximation we considered only the ions that enter the crystal along the ideal line joining atom 2 with the center of the channel. In this particular case p' equals p'' and is given by

$$p'=p''=[(p-1.35\ \mathrm{\AA})^2+(1.92\ \mathrm{\AA})^2]^{1/2}\ . \quad (6)$$

This formula was put into Eq. (5) in order to estimate the electronic energy loss along the [110] channel.

Monte Carlo calculations are more exact than analytical calculations and most of the phenomena involved in ion implantation can be considered. In particular, especially in channeling implants, it is important to consider also the thermal vibrations. The MARLOWE treatment of thermal vibration modes corresponds to a simple model of uncorrelated Gaussian thermal displacements of the lattice atoms, and the mean-square displacement is based on the Debye model. In all cases the thermal displacements of the lattice atoms for implantations at room tem-

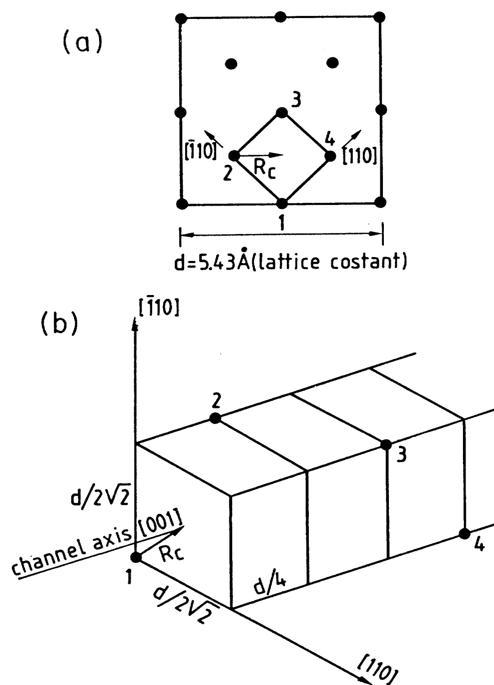

FIG. 9. Configuration of atoms forming the [100] channel in silicon. (a) The channel size and atomic rows. (b) The "spiral configuration" of target atoms around the channel which will be encountered by the projectiles.

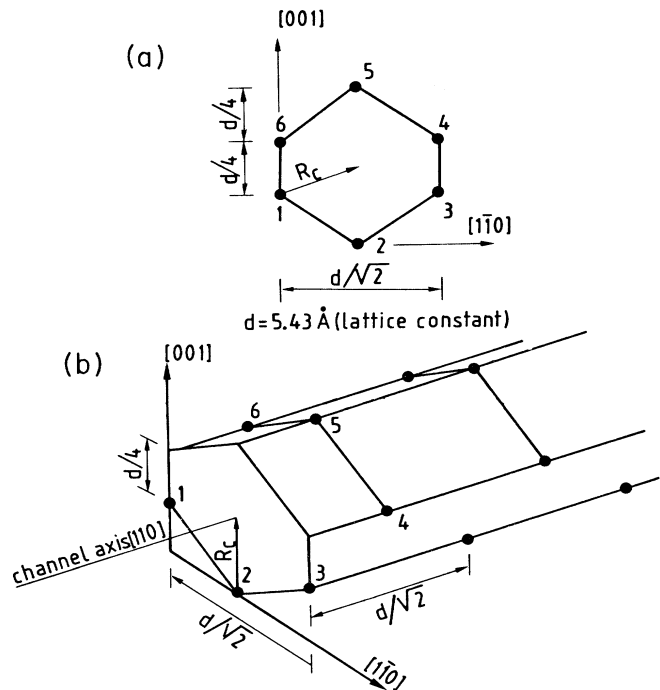

FIG. 10. Configuration of atoms forming the [110] channel in silicon. (a) The channel size and atomic rows. (b) The configuration of target atoms showing the three atoms in each plane originating the "simultaneous collision" described in the text.

perature (300 K) were taken into account by using a Debye temperature of 635 K.[33]

In Figs. 11 and 12 the comparison between the simulated and experimental profiles is shown. Figures 11(a) and 12(a) refer to implants, respectively, at 0.5 and 1 MeV in the amorphous target. The agreement between the experimental and the simulated profiles is excellent. This confirms the right choice of the preexponential factor in Eq. (3). Considering the implants along a crystalline random direction we could obtain a very good agreement too. This proves the ability of Monte Carlo simulations to follow the trajectories if particles are fed in channels. In Figs. 11 and 12 the implanted profiles along the [100] channel are also compared with the simulated distributions. The $R_{\max}$ is well reproduced at the two different energies. This confirms that the choice of the Oen-Robinson impact-parameter formula in the energy range of this work is satisfactory. However the shape of the profile is not perfectly reproduced. For implants in channeling conditions escape from the channel is strongly influenced by the presence of the damage.

MARLOWE considers the recoils and follows their trajectories explicitly within a single cascade, but it does not accumulate damage from an ion to the next ion due to the very large CPU demands. That is, the displacement cascade produced by an ion is reset before the subsequent ion is implanted. Recently some attempts[34–36] have been made to model the introduction of damage in the lattice. However these damage treatments are still in an early development stage and the ability to reproduce the final profile is not yet convincing. If damage is neglected in the simulation very low doses are needed in order to avoid damage at all; typically doses should be $< 10^{12}/\text{cm}^2$ in order to avoid the overlap of successive collision cascades. However it is very difficult to obtain experimental profiles for very-low-dose implants. So the comparison shown in Figs. 11 and 12 between the experimental and simulated channeled profiles is satisfactory. For the implants along the [110] direction, as previously described we used a modified Oen-Robinson formula. Also in this case the $R_{\max}$ is well reproduced and the shapes of the two profiles are comparable. Moreover in the simulations two peaks are clearly distinguishable at the same depth of the corresponding experimental peaks.

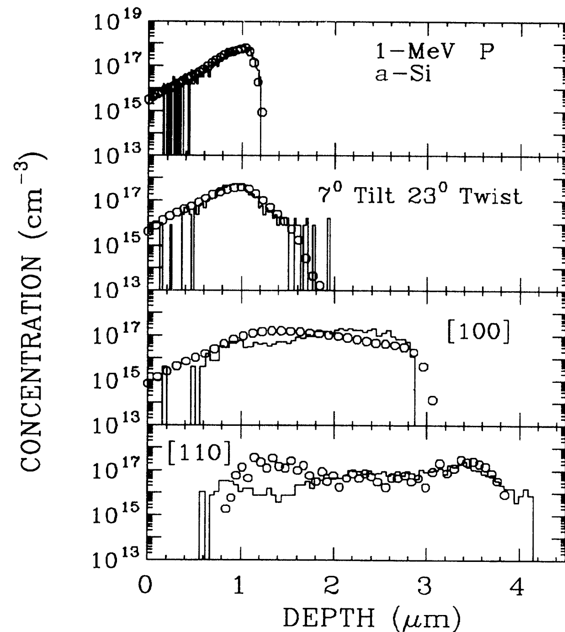

FIG. 12. Same as Fig. 11 but for 1-MeV implants.

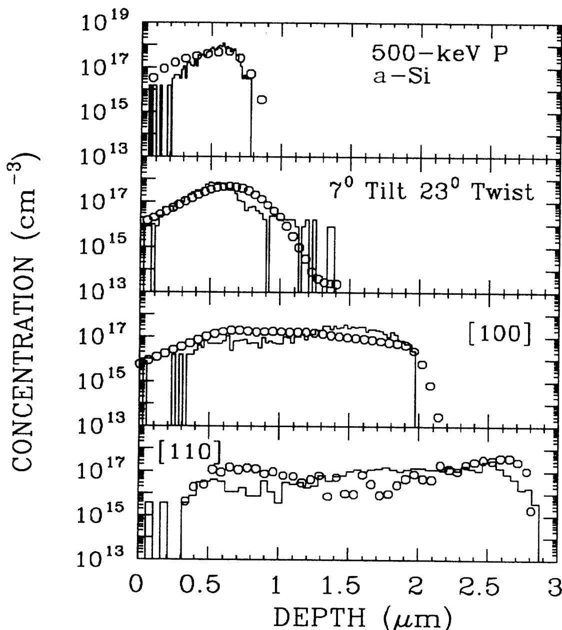

FIG. 11. The experimental profiles obtained implanting 500-keV 2×10^{13} P/cm^2 in different configuration are compared with the distributions obtained by MARLOWE calculations considering 1000 ions. In sequence, implants in amorphous layer, implants in random conditions, implants along the [100] axes, and implants along the [110] axes.

IV. CONCLUSIONS

In the present paper we have presented an extensive study on high-energy P implants in crystal and in amorphous silicon. In implants performed along a random crystalline direction (7° tilt and 23° twist angle) a channeled tail occurs compared with implants performed in amorphous targets. This shows that a relevant feeding-in fraction is present implanting in crystal targets. Channeling implants along the [100] and [110] channels were performed at different doses and energies. At the lower doses flat profiles were obtained with maximum penetration ranges increasing with the square root of the energy. At the higher doses the dechanneled fraction becomes of relevance and was experimentally determined and correlated with the displaced silicon atoms.

The experimental profiles were also simulated by the MARLOWE code. This code was set and partially modified to consider the electron density along different channels.

To account for the electronic energy loss we used the impact-parameter-dependent formula of Oen and Robinson. Though we are in a transition energy range, where many mechanisms contribute to the electronic energy loss, all the data were well reproduced by the electronic stopping used. The presence of multiple interactions with the atoms of the [110] channel was taken into account by changing appropriately the Oen-Robinson formula. All the obtained experimental profiles were compared with the distributions obtained by MARLOWE simulations showing an excellent agreement.

ACKNOWLEDGMENTS

We wish to acknowledge Dr. Salvo Coffa and Dr. Dale C. Jacobson of AT&T Bell Laboratories for providing the 2-μm-thick Si amorphous layers. We are also indebted to Orazio Parasole for his invaluable technical support. We acknowledge the Solid State Division of Oak Ridge National Laboratory for providing a copy of the MARLOWE code. This work has been supported in part by the EUREKA project and in part by Piano Nazionale per la Microelettronica.

*Permanent address: Centro Nazionale per la Ricerca e lo Sviluppo dei Materiali, Via Marconi 147, I 72023 Mesagne, Brinosili, Italy.

[1]P. Spinelli, A. M. Cartier, and M. Bruel, Nucl. Instrum. Methods B **21**, 452 (1987).

[2]D. C. Ingram, Nucl. Instrum. Methods B **12**, 161 (1985).

[3]G. Galvagno, A. Cacciato, F. Benyaich, V. Raineri, F. Priolo, E. Rimini, S. Capizzi, and P. Romano, Mater. Sci. Eng. B (to be published).

[4]D. C. Ingram, J. A. Baker, D. A. Walsh, and E. Strathman, Nucl. Instrum. Methods B **21**, 460 (1987).

[5]R. J. Schreutelkamp, F. W. Saris, J. F. M. Westendorp, R. E. Kaim, G. B. Odlum, and K. T. F. Janssen, Mater. Sci. Eng. B **2**, 139 (1989).

[6]R. J. Schreutelkamp, V. Raineri, F. W. Saris, R. E. Kaim, J. F. M. Westendorp, P. F. H. M. van der Meulen, and K. T. F. Janssen, Nucl. Instrum. Methods B **55**, 615 (1991).

[7]M. Posselt and W. Skorupa, Nucl. Instrum. Methods B **21**, 8 (1987).

[8]R. J. Schreutelkamp, J. R. Liefting, P. M. Zagwijn, W. X. Lu, and F. W. Saris, Nucl. Instrum. Methods B **48**, 448 (1990).

[9]R. J. Schreutelkamp, J. R. Liefting, P. M. Zagwijn, W. X. Lu, and F. W. Saris, Nucl. Instrum. Methods B **47**, 329 (1990).

[10]S. P. Ahlen, Rev. Mod. Phys. **52**, 121 (1980).

[11]J. Lindhard and M. Scharff, Phys. Rev. **124**, 128 (1961).

[12]Ya. A. Teplova, V. S. Nikolae, I. S. Dmitriev, and L. N. Fateeva, Zh. Eksp. Teor. Fiz. **42**, 383 (1962) [Sov. Phys.—JETP **15**, 31 (1962)].

[13]K. Dettmann and M. T. Robinson, Phys. Rev. B **10**, 1 (1974).

[14]A. Desalvo and R. Rosa, J. Phys. C **10**, 1595 (1977).

[15]G. G. Bentini, M. Bianconi, R. Nipoti, F. Malaguti, and E. Verandini, Nucl. Instrum. Methods B **53**, 1 (1991).

[16]M. T. Robinson and I. M. Torrens, Phys. Rev. B **9**, 5008 (1974).

[17]V. Raineri, G. Galvagno, E. Rimini, J. Biersack, S. T. Nakagawa, A. La Ferla, and A. Carnera, Radiat. Eff. **116**, 211 (1991).

[18]W. K. Chu, J. W. Mayer, and M.-A. Nicolet, *Backscattering Spectrometry* (Academic, New York, 1978).

[19]Y. L. Khait, R. Brener, and R. Beserman, Phys. Rev. B **38**, 6107 (1988).

[20]V. Raineri, R. J. Schreutelkamp, F. W. Saris, K. T. F. Janssen, and R. E. Kaim, Appl. Phys. Lett. **58**, 922 (1991).

[21]M. Servidori, R. Angelucci, F. Cembali, P. Negrini, S. Solmi, P. Zaumseil, and U. Winter, J. Appl. Phys. **61**, 1834 (1987).

[22]W. Vandervost and T. Clarysse, J. Electrochem. Soc. **137**, 679 (1990).

[23]T. Clarysse, W. Vandervost, and A. Casel, Appl. Phys. Lett. **57**, 2857 (1990).

[24]H. L. Berkowitz and X. Lux, J. Electrochem. Soc. **18**, 1137 (1981).

[25]W. R. Thurber, R. L. Mattis, and Y. M. Liu, Natl. Bur. Stand. (U.S.) Spec. Publ. No. 400-464 (U.S. GPO, Washington, D.C., 1981).

[26]B. R. Appleton, C. Erginsoy, and W. M. Gibson, Phys. Rev. **131**, 330 (1967).

[27]M. T. Robinson (unpublished).

[28]M. Hou and M. T. Robinson, Nucl. Instrum. Methods **132**, 641 (1976).

[29]O. S. Oen and M. T. Robinson, Nucl. Instrum. Methods **132**, 647 (1976).

[30]J. Lindhard, M. Sharff, and H. E. Schiott, K. Dan. Vid. Selks. Mat. Fys. Medd. **33**, No. 14 (1963).

[31]J. P. Biersack and L. G. Haggmark, Nucl. Instrum. Methods **174**, 647 (1980).

[32]J. P. Biersack, G. Schiwietz, P. Grande, and M. Behar, Phys. Lett. A (to be published).

[33]G. Burns, *Solid State Physics* (Academic, New York, 1985).

[34]T. L. Crandle and B. J. Mulvaney, IEEE Electron Device Lett. **11**, 42 (1990).

[35]H. J. Kang, R. Shimizu, T. Saito, and H. Yamakawa, J. Appl. Phys. **62**, 2733 (1987).

[36]K. M. Klein, C. Park, and Al F. Tasch, Tech. Dig.—Int. Electron Devices Meet. **XX**, 745 (1990).